A&A 604, A21 (2017)
DOI: 10.1051/0004-6361/201730964

Astronomy & Astrophysics

New JVLA observations at 3 GHz and 5.5 GHz of the "Kite" radio source in Abell 2626

A. Ignesti[1,2], M. Gitti[1,2], G. Brunetti[2], L. Feretti[2], and G. Giovannini[1,2]

[1] Dipartimento di Fisica e Astronomia, Università di Bologna, via Gobetti 93/2, 40129 Bologna, Italy
e-mail: myriam.gitti@unibo.it
[2] INAF, Istituto di Radioastronomia di Bologna, via Gobetti 101, 40129 Bologna, Italy

Received 10 April 2017 / Accepted 26 April 2017

ABSTRACT

Context. We report on new *Karl Jansky* Very Large Array (JVLA) observations performed at 3 GHz and 5.5 GHz of Abell 2626. The cluster has been the object of several studies in recent years due to its peculiar radio emission, which shows a complex system of symmetric radio arcs characterized by a steep spectrum. The origin of these radio sources is still unclear. Due to their mirror symmetry toward the center, it has been proposed that they may be created by pairs of precessing jets powered by the inner active galactic nuclei (AGN).
Aims. The new JVLA observations were requested with the specific aim of detecting extended emission on frequencies higher than 1.4 GHz, in order to constrain the jet-precession model by analyzing the spectral index and radiative age patterns along the arcs.
Methods. We performed a standard data reduction of the JVLA datasets with the software CASA. By combining the new 3 GHz data with the archival 1.4 GHz VLA dataset we produced a spectral index map of the extended emission, and then estimated the radiative age of the arcs by assuming that the plasma was accelerated in moving hot-spots tracing the arcs.
Results. Thanks to the high sensitivity of the JVLA, we achieve the detection of the arcs at 3 GHz and extended emission at 5.5 GHz. We measure a mean spectral index <-2.5 for the arcs up to 3 GHz. No clear trend in spectral index or radiative age is detected across the arcs, which may challenge the interpretation based on precession or put strong constraints on the jet-precession period. In particular, by analyzing the radiative age distribution along the arcs, we were able to provide for the first time a timescale <26 Myr of the jet-precession period.

Key words. radiation mechanisms: non-thermal – galaxies: clusters: individual: Abell 2626 – galaxies: individual: IC 5338 – galaxies: individual: IC 5337 – galaxies: jets – radio continuum: galaxies

1. Introduction

In recent years, radio observations have revealed that a fraction of galaxy clusters host diffuse synchrotron emission on cluster scale. The discovery of radio sources not associated with any individual galaxy proves the presence of non-thermal components, such as relativistic particles and magnetic fields, mixed with the thermal intra-cluster medium (ICM) on spatial scales that are comparable to the cluster size. According to their morphology and location in the cluster, cluster-scale radio sources are classified as radio relic, radio halos and radio mini-halos (e.g., Feretti et al. 2012). Relics are polarized, elongated, arc-shaped synchrotron sources located in the peripheries of dynamically disturbed clusters. Radio relics are also unique probes of the properties of magnetic fields in the outskirts of galaxy clusters. Halos and mini-halos are, instead, roundish radio sources located in the cluster central regions. The two classes differ in size and in the dynamical properties of the hosting clusters. Radio halos are located in the center of dynamically disturbed clusters show signs of recent major merger activity, whereas mini-halos are detected only in relaxed, cool-core clusters. It is currently thought that relics and halos originate from complex acceleration mechanisms that are driven by shocks and turbulence in the ICM (e.g., Brunetti & Jones 2014). On the other hand, the mini-halo diffuse emission is always observed to surround the intense radio emission of the brightest cluster galaxy (BCG), which often shows non-thermal radio jets and lobes ejected by the central active galactic nucleus (AGN). The radio-lobe plasma strongly interacts with the ICM by inflating large X-ray cavities and triggering the so-called 'radio-mode AGN feedback (e.g., Gitti et al. 2012). The central radio-loud AGN is also likely to play a role in the initial injection of the relativistic particles emitting in the mini-halo region. Nonetheless, the diffuse radio emission of mini-halos is truly generated from the ICM on larger scales, where the thermal and non-thermal components are mixed, and can be explained in the framework of leptonic models that envision in situ particle re-acceleration by turbulence in the cool-core region (e.g., Gitti et al. 2002). Turbulence in cool cores may be generated by several mechanisms, including the interplay between the outflowing relativistic plasma in AGN jets/lobes, and sloshing gas motions.

This work is a multi-frequency study of the inner part of Abell 2626 (hereafter A2626), which was included in the first sample of mini-halo clusters (Gitti et al. 2004). Its radio morphology, more complex than that of the standard radio bubbles typically observed to fill X-ray cavities, represents a challenge to models for the ICM / radio source interaction in cool cores. A2626 is a low-redshift (z = 0.0553 Struble & Rood 1999), regular poor cluster (Mohr et al. 1996), located at RA 23h36m30s, DEC+21d08m33s and is part of the Perseus-Pegasus supercluster. A2626 has an estimated mass of 1.3×10^{15} $M_{\odot}$ and a virial radius of 1.6 Mpc (Mohr et al. 1996). It is a cool-core

cluster with estimated X-ray luminosity of 1.9×10^{44} erg s^{-1} and a mass accretion rate of 4 $M_{\odot}$ yr^{-1} (Bravi et al. 2016). Its core-dominant (cD) galaxy IC 5338 hosts a pair of optical nuclei with a projected separation of 3.5 arcsec, of which only the southern one has a counterpart also in the radio (Gitti 2013, hereafter G13) and hard X-ray (Wong et al. 2008) bands (see Wong et al. 2008, Fig. 3). The extended radio emission of the cluster has a peculiar morphology resembling a giant kite, with striking arc-like, symmetric features whose origin is puzzling (Gitti et al. 2004; Gitti 2013; Kale & Gitti 2017). The arcs are collimated structures with a maximum length of ≃70 kpc, steep radio spectrum ($\alpha < -2.5$[1], Kale & Gitti 2017), and no evidence of polarized emission (G13). Gitti et al. (2004) argued that the elongated features are distinct from and embedded in the diffuse, extended radio emission, which they classified as a radio mini-halo and successfully modeled as radio emission from relativistic electrons reaccelerated by MHD turbulence in the cool-core region. On the other hand, the origin and nature of the radio arcs are still unclear. Their morphology may suggest that the arcs are radio bubbles or cluster relics. However, *Chandra* and *XMM-Newton* observations failed to detect any X-ray cavity or shock front associated to them, in general showing no clear spatial correlation between the non-thermal emission of the arcs and the thermal emission of the cluster (Wong et al. 2008).

Wong et al. (2008) argued that the peculiar radio morphology of the northern and southern arcs may be produced by jet precession triggered by the reciprocal gravitational interactions of the two cores of the cD galaxy. According to this scenario, the relativistic plasma of the arcs was accelerated in a pair of precessing hot-spots powered by the AGN located inside the southern core of IC 5338. In particular, if two jets, ejected towards the north and south directions, are precessing about an axis that is nearly perpendicular to the line-of-sight and are stopped at approximately equal radii from the AGN (at a "working surface"), radio emission may be produced by particle acceleration, thus giving rise to the elongated structures. The impressive arc-like, mirror symmetric morphology of these features highlighted by the high-resolution radio images (G13) may support this interpretation. On the other hand, the recent discovery of the third and fourth radio arc to the east-west direction (Gitti 2013; Kale & Gitti 2017) further complicates the picture. They could represent other radio bubbles ejected in a different direction, similarly to what has been observed in RBS 797 (Doria et al. 2012; Gitti et al. 2013), but again the absence of any correlation with the X-ray image disfavors this interpretation. In the model proposed by Wong et al. (2008), they could represent the result of particle acceleration produced at a working surface by a second pair of jets ejected to the east-west direction. This interpretation would imply the existence of radio jets emanating also from the northeast nucleus of the cD galaxy IC 5338, which, however, does not show a radio core.

In order to constrain the jet-precession scenario, we requested new *Karl Jansky* Very Large Array (JVLA) observations at 3 GHz and 5.5 GHz to estimate the spectral index distribution along the arcs and thus infer detailed information on the radiative age of the plasma in the radio arcs. According to the jet-precession model, due to the gradual formation of the structures, the plasma along the arcs should exhibit a monotonic trend from one end to the other in the radiative age distribution, and thus also in the spectral index. The differences in radiative age between the opposite ends of each arc would represent a measure of the time required to create the arcs, and therefore it would also provide an estimate of the precession time of the jets.

We adopt a ΛCDM cosmology with $H_0 = 70$ km s^{-1} Mpc^{-1}, $\Omega_M = 1 - \Omega_\Lambda = 0.3$. The cluster luminosity distance is 246.8 Mpc, and the angular scale is of 1 arcsec = 1.1 kpc[2].

Table 1. New JVLA data analysed in this work (project code: 14B-022).

PI: Dr. Myriam Gitti	5.5 GHz [C-band]	3 GHz [S-band]
Observation date	19-Oct.-2014	14-Dec.-2014
Frequency coverage (GHz)	4.5–6.5	2.0–4.0
Array configuration	C	C
On source time	44 m	63 m

Notes. A JVLA standard dataset is parted in 16 spectral windows (spw) with a bandwidth of 128 MHz. Each spw is, in turn, divided in 64 channels with a channelwidth of 2 MHz.

2. Observation and data reduction

We performed new observations of the radio source A2626 at 3 GHz and 5.5 GHz with the JVLA in C-configuration (see Table 1 for details regarding these observations). In all observations, the source 3C 48 (J0137+3309) was used as the primary flux density calibrator, while the sources J0016−0015 and 3C 138 (J0521+1638) were used as secondary phase and polarization calibrators, respectively. Data reduction was done using the National Radio Astronomy Observatory (NRAO) Common Astronomy Software Applications package (CASA), version 4.6. As a first step we carried out a careful editing of the visibilities. In particular, the 3 GHz dataset required an accurate flagging to remove every radio frequency interference (RFI), which is quite common in this radio band. Overall, we removed about 10% of the visibilities in the 5.5 GHz dataset and 20% in the 3 GHz one by repeating manual and automatic flagging with the modes `MANUAL` and `RFLAG` of the CASA task `FLAGDATA`. Due to the visibility loss, the bandwidth of the 3 GHz observation decreased from 2.0 GHz (2.0–4.0 GHz) to 1.6 GHz (2.4–4.0 GHz), thus moving the central frequency from 3.0 GHz to 3.2 GHz. We performed a standard calibration procedure[3] for each dataset, and the target was further self-calibrated.

Due to the presence of several bright radio sources in the field of view, we carried out the imaging procedure with the task `CLEAN`, on a $32' \times 32'$ region centered on the cluster in order to remove as best as possible their secondary lobes. To this end, we used `gridmode = WIDEFIELD` to parametrize the curvature of the sky regions far from the phase center. We also used the MS-MFS algorithm (Rau & Cornwell 2011) by setting a two-terms approximation of the spectral model (`nterms = 2`) and the multi-scale clean (`multiscale = [0,5]` on the point-like and beam scales) to reconstruct as best as possible the faint extended emission.

3. Results

We report here the most relevant results of our analysis. For each observing band, we produced three different types of maps by varying the relative weight between short

[1] In this work the radio spectral index α is defined such as $S \propto \nu^{\alpha}$.

[2] http://www.astro.ucla.edu/#7Ewright/CosmoCalc.html

[3] E.g., see the Tutorials, https://casaguides.nrao.edu/index.php/

and long baselines. The UNIFORM maps, obtained by setting weighting = UNIFORM, nterms = 1, give a uniform weight to all spatial frequencies, thus enhancing angular resolution. The NATURAL maps, obtained by setting weighting = NATURAL, nterms = 1, give more weight to low spatial frequencies thus degrading angular resolution but at the same time maximizing the sensitivity to the diffuse, extended emission sampled by short baselines. Finally, the ROBUST 0 maps, obtained by setting weighting = BRIGGS, ROBUST = 0, nterms = 2, have resolution and sensitivity half-way between UNIFORM and NATURAL. We report the maps in Fig. 1 (5.5 GHz) and Fig. 2 (3 GHz), whereas the flux density values measured on each map are reported in Table 2. Typical amplitude calibration errors are at 3%, therefore we assume this uncertainty on the flux density measurements. In the following analysis we assume the 7 × rms levels at 1.4 GHz (shown in red in Fig. 2, middle panel) as reference contours for the size and position of the arcs and of the unresolved core, as they best trace the morphology of the features seen at 1.4 GHz (G13).

3.1. 5.5 GHz maps

The published map at 4.8 GHz (G13) does not show diffuse radio emission or discrete features like the radio arcs seen at 1.4 GHz. The new observations presented in this work were performed with a more compact configuration of the array and with the larger receivers band of the JVLA, thus reaching an unprecedented high sensitivity. This allowed us to detect faint extended emission around IC 5338 and IC 5337 for the first time at 5.5 GHz.

We report the 5.5 GHz maps in Fig. 1. The UNIFORM (top panel) and the ROBUST 0 (middle panel) maps, which have a resolution of 2″.8 × 2″.7 and 3″.2 × 2″.8, do not show extended emission around IC 5338, except for the jet-like feature in the south-west, which was also observed at 1.4 GHz by G13. On the other hand, in the ROBUST 0 map the close source on the left, IC 5337, exhibits an extended emission in addition to the radio core already detected by G13. Due to its optical properties indicating that the galaxy is leaving a trail of cold gas, IC 5337 has also been classified as a jellyfish galaxy (Poggianti et al. 2016). Therefore, the disrupted radio morphology agrees with previous dynamical studies of the cluster (Mohr et al. 1996) indicating that IC 5337 is moving toward IC 5338.

In the bottom panel of Fig. 1 we show the NATURAL map at a resolution of 4″.9 × 4″.4, obtained by further imposing a UV tapering to 20 kλ to maximize the sensitivity to the short spatial frequencies. In this high-sensitivity, low-resolution image we detected extended emission around IC 5338. The emission region extends up to 27″ (∼30 kpc) and is located inside the radio arcs known at 1.4 GHz (G13). We measure a total flux density of $S_{5.5,\mathrm{NAT}} = 8.2 \pm 0.2$, of which 6.2 ± 0.2 mJy are contributed by the core, thus leaving an estimate of 2.0 ± 0.3 mJy related to the extended emission. The nature of this radio emission is uncertain. On the one hand, due to its position, it may be contributed by the emission of the radio arcs and of the inner AGN jets. On the other hand, it may indicate the presence of a diffuse radio mini-halo.

We note that the core flux density measured in these new 5.5 GHz maps differs from that reported by G13 in the same band, which is 9.6 ± 0.3 mJy. We accurately checked the flux calibration procedure in both observations finding no trivial problems, therefore this ≈40% flux difference may indicate variability, and therefore activity, of the IC 5338 core. By observing hard X-ray emission from its core, Wong et al. (2008) suggested that

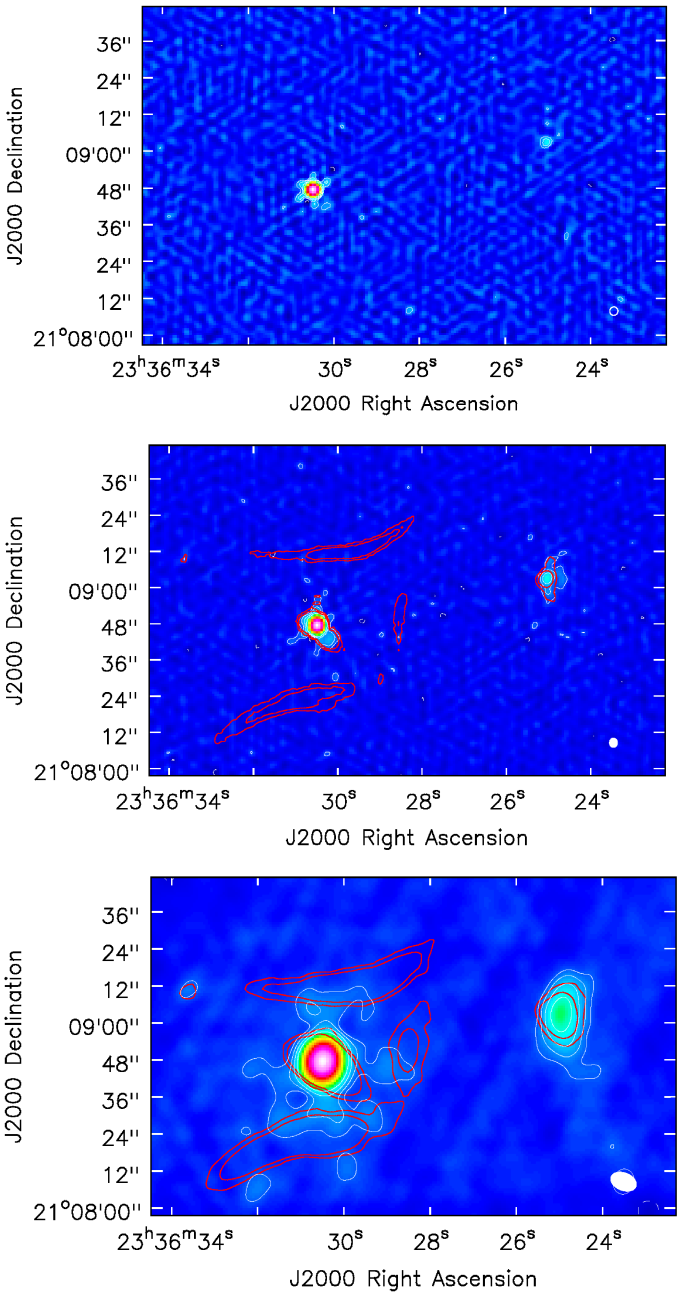

Fig. 1. *Top panel*: 5.5 GHz map (UNIFORM) at a resolution of 2″.8 × 2″.7 with rms noise of 16.1 μJy beam^{-1}. *Middle panel*: 5.5 GHz map (ROBUST 0) at a resolution of 3″.2 × 2″.8 with rms noise = 8.0 μJy beam^{-1}. *Bottom panel*: 5.5 GHz map (NATURAL, UVTAPER = [0,20]) at a resolution of 4″.9 × 4″.4 with rms noise = 8.6 μJy beam^{-1}. In all panels the white contour levels are –3, 3, 6, 12, 24 × rms noise, the red ones are the 7, 14 × rms of 1.4 GHz maps produced with comparable resolution from G13 data. The rms levels of the red contours are 15.4 and 21.9 μJy beam^{-1} in the *middle and bottom panel*, respectively.

IC 5338 hosts an AGN. The jet-like features observed at 1.4 GHz by G13 and the likely variability of the radio emission that we observe are consistent with this hypothesis.

3.2. 3 GHz maps

The 2.0–4.0 GHz band is the new radio window observed with the JVLA. This is also the transmission band of the

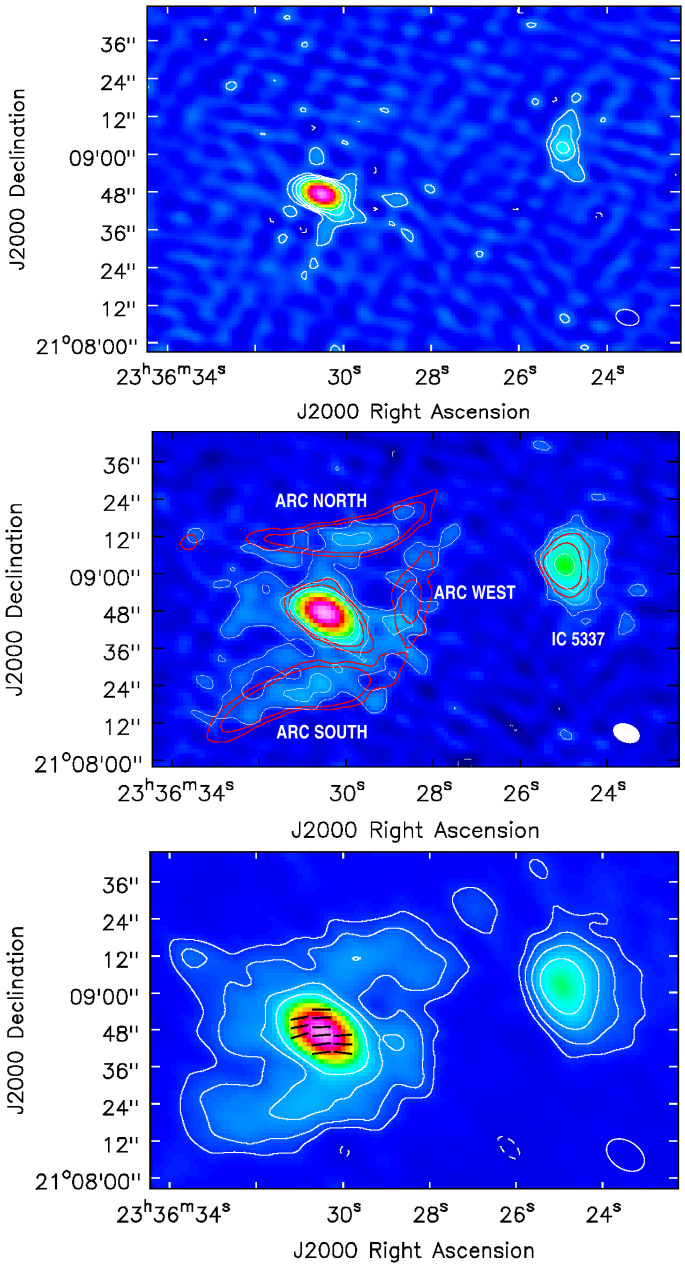

Fig. 2. *Top panel*: 3 GHz map (UNIFORM) at a resolution of 7″.5 × 8″.5 with rms noise = 40.1 μJy beam^{-1}. *Middle panel*: 3 GHz map (ROBUST 0) at a resolution of 8″.7 × 5″.8, and rms noise = 20.4 μJy beam^{-1}. *Bottom panel*: 3 GHz map (NATURAL, UVTAPER = [0,20]) at a resolution of 13″.1 × 8″.5, and rms noise = 18.5 μJy beam^{-1}. In black there are the polarization vectors. In all panels the white contour levels are –3, 3, 6, 12, 24 × rms noise in all maps, the red ones are the 7, 14 × rms of 1.4 GHz maps made with comparable resolution.The rms levels of the red contours are 21.9 μJy beam^{-1}.

communication satellites, so it is populated by radio interferences that may jeopardize the observations. The maps we present here have been produced after an accurate editing of the target visibilities. The UNIFORM map (Fig. 2, top panel) exhibits only the emission of IC 5338 and the extended emission of IC 5337. The ROBUST 0 map at a resolution of 8″.7 × 5″.8 (Fig. 2, middle panel) shows several patches of extended emission. By superposing the 1.4 GHz contours by G13 (in red), we confirm that the new features detected in this band are the radio arcs already seen at 1.4 GHz. Remarkably, we identify a feature to the east

Table 2. Flux density values of the radio sources of A2626, measured on the maps of Figs. 1, 2 inside the 3 × rms contours of each map.

Weighting	Component	Flux density [mJy]
5.5 GHz maps (Fig. 1)		
UNIFORM	Total	6.7 ± 0.2
	Core	6.7 ± 0.2
	IC 5337	0.2 ± 0.1
ROBUST 0	Total	7.4 ± 0.2
	Core	6.0 ± 0.2
	IC 5337	0.5 ± 0.1
NATURAL	Total	8.2 ± 0.2
	Core+jets	6.2 ± 0.2
	IC 5337	0.5 ± 0.1
3 GHz maps (Fig. 2)		
UNIFORM	Total	12.1 ± 0.5
	Core+jets	11.7 ± 0.4
	IC 5337	1.6 ± 0.3
ROBUST 0	Total	14.6 ± 0.4
	Core+jets	12.0 ± 0.4
	Arc Noth	0.4 ± 0.1
	Arc South	0.5 ± 0.1
	Arc West	0.5 ± 0.1
	IC 5337	1.5 ± 0.1
NATURAL	Total	16.5 ± 0.5
	Core+jets	10.9 ± 0.3
	Arc Noth	0.7 ± 0.1
	Arc South	0.8 ± 0.1
	Arc West	0.4 ± 0.1
	IC 5337	2.2 ± 0.1

that resembles the diffuse emission detected by G13 (see their Fig. 3), but does not coincide entirely with the eastern arc discovered by Kale & Gitti (2017). Due to the low resolution of this map, the inner part of IC 5338 is unresolved.

For this band, we also produced a polarization intensity map. We combined the stokes components, Q and U, of the emission to compute the vector and total intensity maps of linear polarization. We set the weights to NATURAL to improve the signal-to-noise ratio (SNR) of the arcs. The NATURAL map in Fig. 2, bottom panel, shows an overlay of polarization vector and total intensity contours. We observe only a small percentage (~2%) of polarized emission from the core, whereas we do not observe polarized emission from the arcs. By comparing the rms of the polarized emission map with the peak flux density of the arcs, we estimate an upper limit for the polarized emission fraction of the arcs of ~30%. However, we note that the low-resolution map is affected by the beam depolarization effect, so high-resolution observations are needed to confirm the lack of polarized emission from the radio arcs at 3 GHz.

3.3. Spectral index maps

By combining the new JVLA observation at 3 GHz with the VLA ones at 1.4 GHz obtained with the VLA in A+B configuration (G13), we produced a spectral index map of the extended emission of A2626. We produced the input maps by setting weighting = UNIFORM, UVRANGE = 0-40,

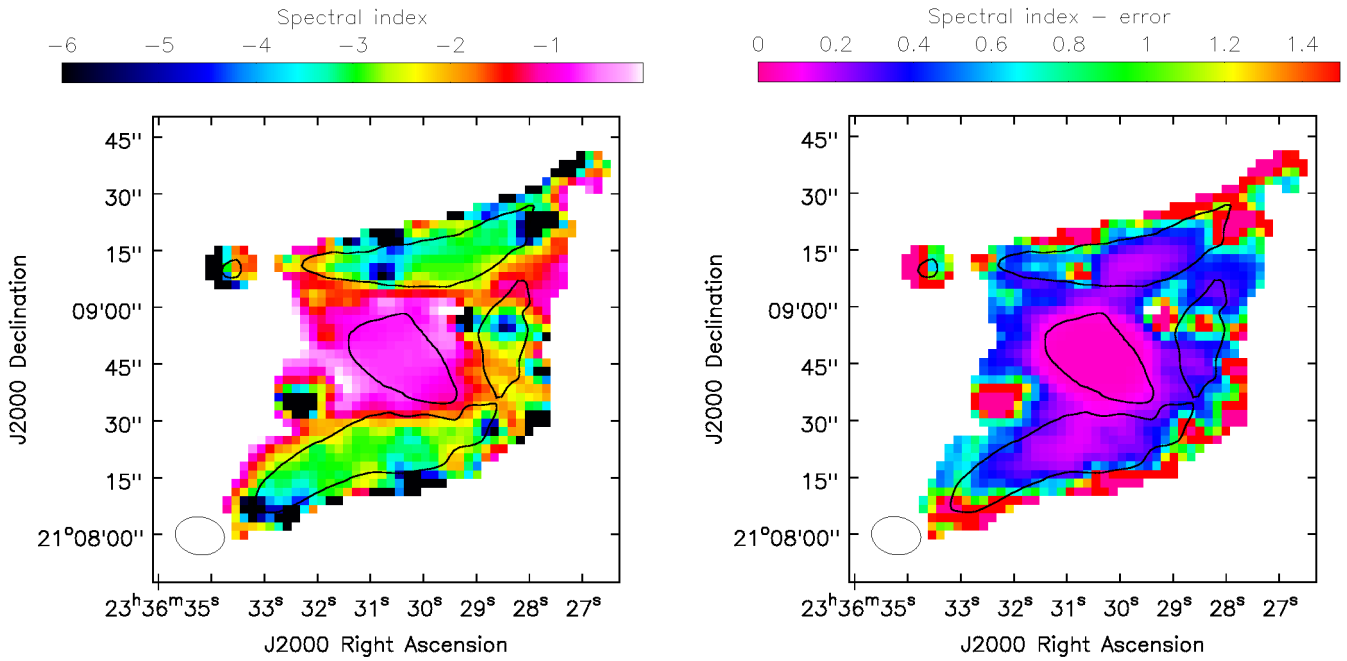

Fig. 3. Bandwidth-corrected spectral index map (*left*) and relative-error map (*right*) obtained from the 1.4 GHz and 3 GHz dataset. The black contours are the same 1.4 GHz contours reported in Fig. 2, *middle panel*.

`UVTAPER=0-20, RESTORINGBEAM=13″×10″, nterms=1, multiscale=[0,5]`. We improved the sensitivity to the faint, extended emission of the `UNIFORM` maps by applying a `UVTAPER` and by enlarging the beam to improve the SNR. The rms of the 1.4 GHz and 3 GHz maps are 31.9 and 29.1 μJy beam^{-1}, respectively.

In calculating the spectral index value in each pixel of the map, we excluded regions where the 1.4 GHz brightness is <3× rms level. We further corrected the spectral index map for the bandwidth effect described by Condon (2015). Due to the large receiver bandwidth of the JVLA, the flux density the we measure on the 3 GHz maps may not coincide with the flux at 3.2 GHz, which is the arithmetical center of our band, but instead it may be the flux density at an equivalent frequency, ν_u, defined as:

$$\nu_u = \left[\frac{1}{\alpha+1}\left(\frac{\nu_{\rm max}^{\alpha+1}-\nu_{\rm min}^{\alpha+1}}{\nu_{\rm max}-\nu_{\rm min}}\right)\right]^{1/\alpha}, \quad (1)$$

where $\nu_{\rm max}$ and $\nu_{\rm min}$ (expressed in GHz) are the ends of the bandwidth and α is the spectral index. According to this relation, ν_u is a function of α, which is, in turn, a function of the frequencies. In order to correct the spectral index map, which was computed between 1.4 and 3.2 GHz, we numerically derived the correction for the spectral indices. According to our bandwidth (2.4–4.0 GHz), we estimated a first set of equivalent frequencies ν_u^i for a set of spectral indices α_i between –0.1 and –7.0. We then corrected the spectral indices for the equivalent frequencies, thus obtaining a new set α_{i+1} that allowed us to estimate again a new set of equivalent frequencies ν_u^{i+1}. We repeated this cycle until it converges to the final values ν_u^N and α_N. We then obtained by numerical fit the relation $\alpha_N(\alpha_i)$ that we finally applied to each pixel of the uncorrected spectral index map with the task `immath` of CASA. With the $\alpha_N(\alpha_i)$ relation we also re-scaled the relative spectral index error map. We report both the corrected spectral index map and the relative error map in Fig. 3.

The spectral index map disentangles the extended emission into two major components, the unresolved core with a flat spectral index[4] and the arcs with steep spectral index $\alpha < -2.5$, that is consistent with the recent results by Kale & Gitti (2017). We measured the mean spectral index inside the 1.4 GHz reference contours (Fig. 2, middle panel) for the northern, southern, and western arcs, finding $\alpha = -3.2 \pm 0.6$, -3.0 ± 0.4 and -2.6 ± 0.6, respectively. The unresolved core has a mean spectral index $\alpha = -0.7 \pm 0.1$.

3.4. Radiative age maps

The continuous radiative loss modifies the spectrum of the emitting particles by steepening it. By considering only the effect of radiative losses on the evolution of the energy of electrons, it is possible to estimate the radiative age, $t_{\rm rad}$, of the emitting plasma from the break frequency, $\nu_{\rm br}$, of its synchrotron spectrum and the magnetic field, B, that produces the radio emission (e.g., Eq. (2) of Murgia et al. 1999). From this relation, it is possible to demonstrate that the radiative life-span, for a given $\nu_{\rm br}$, is maximized by a magnetic field $B_{ml} = B_{\rm CMB}/\sqrt{3}$ μG, where $B_{\rm CMB} = 3.25(1+z)^2$ μG is the equivalent magnetic field of the inverse Compton emission and z is the redshift of the radio source. By numerically integrating the synchrotron emission spectrum, we derived a $t_{\rm rad}(\alpha)$ relation for a population of particles with an energy distribution function $n(E) \propto E^{-\Gamma}$, and a magnetic field B that is uniform and constant over the radio source. We assumed a $B = B_{ml} = 2.1$ μG as magnetic field, and $\Gamma = 2.4$ for the energy distribution function, which we derived from the hypothesis of the jet-precession model. If the plasma of the arcs was initially accelerated in a hot-spot, then it had an initial spectral index $\alpha = -0.7$ (e.g. Meisenheimer et al. 1997), and so $\Gamma = 1 - 2\alpha = 2.4$. Therefore, the $t_{\rm rad}$ map exhibits the upper limit of the time required for the spectrum to steepen from -0.7 to the values that we observe in Fig. 3. Due to our assumptions,

[4] As a word of caution we note that the spectral index in the central region may be unreliable due to the core variability, because the observations are separated by five years.

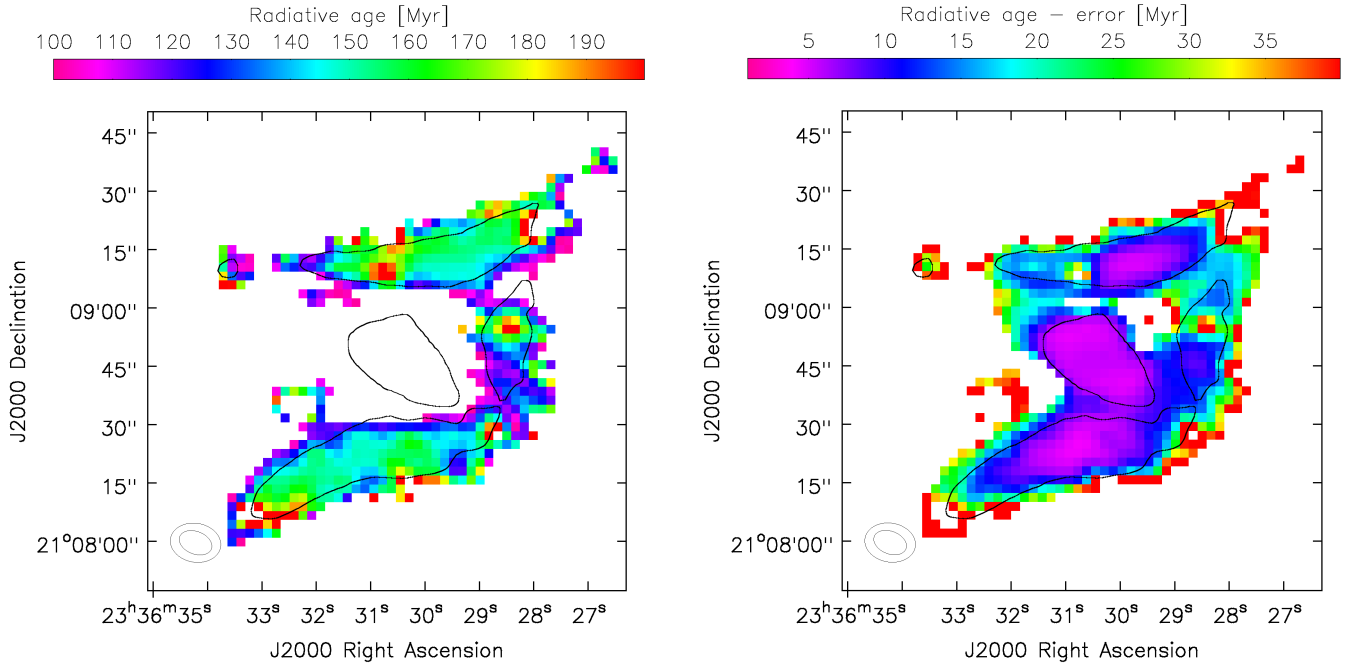

Fig. 4. Radiative age map (*left*) and relative error map (*right*) obtained from Fig. 3 by assuming $B = 2.1$ μG and $\Gamma = 2.4$. The black contours are the same 1.4 GHz contours reported in Fig. 2, *middle panel*. The map displays the upper limit of the time required to steepen the spectral index of the synchrotron emission from −0.7 to the value reported in Fig. 3.

it was not possible to evaluate the $t_{\rm rad}$ in those regions that emit with a spectral index flatter than −0.7.

We computed the spectral map in Fig. 3 with the $t_{\rm rad}(\alpha)$ relation and we obtained the radiative age map. Moreover, we obtained the relative error map on the radiative age from the spectral index error map by estimating the radiative age associated to the upper and lower limits of the spectral index map. We report the radiative age map and the relative error map in Fig. 4. To obtain an indicative estimate of the mean upper limit on the radiative age, we averaged the values of the $t_{\rm rad}$ map inside the 1.4 GHz reference contours (Fig. 2, middle panel). We measured $t_{\rm rad}$ = 157 Myr, 148 Myr, and 136 Myr for the northern, southern, and western arcs, respectively, which can be considered as an estimate of the maximum time elapsed since the particle acceleration. The average radiative age error, σ_t, on those regions is ∼12 Myr.

4. Discussion

The new JVLA observations presented in this work add important information to the general picture of A2626, and allow us to test the jet-precession model for the first time.

The spectral index map in Fig. 3 exhibits the arcs as steep-spectrum radio sources, with $\alpha \leq -2.5$. We do not observe $\alpha \simeq -0.7$ at any of the arc ends, which should be the initial spectral index of the plasma. We therefore argue that the activity has ceased. The radiative map that we provide (Fig. 4) does not show the real age of the arcs, but only its upper limit, because we do not know the real strength of the magnetic field in the arc regions. However, it is useful to constrain the time-scale of the jet precession by considering the difference between the radiative age at the ends of each arc, $\Delta t_{\rm rad}$. This can be considered as a measure of the time required by the jets to cover the arc length, thus it is an estimate of the timescale of the precession period of the jets.

According to the jet-precession scenario, the relativistic plasma of the arcs was accelerated gradually along the structures by a pair of precessing jets. Therefore, the spectral index distribution along the arcs may reflect the gradual formation of the structures by showing a monotonic steepening trend from one end to the other, where the emission with the flattest spectral index comes from the most recently accelerated plasma. Moreover, the trends along the northern and southern arcs should be anti-symmetric due to the geometry of the jet-precession (if the northern arc is created from west to east, then the southern arc must be created from east to west), and they should be observable also in the radiative age maps.

Observationally, the spectral index map (Fig. 3) does not show any clear evolution in the spectrum along the arcs, hinting at the absence of the age progression expected by the precession model. In order to quantitatively confirm this result, we sampled both the spectral index and the radiative age maps with the sampling reported in Fig. 5 (bottom-right panel) and we measured the values, with the relative errors, of each sample. The samples are as large as the beam (13″ × 10″) and cover the area delimited by the 1.4 GHz reference contours shown in Fig. 2, middle panel. We report the result of our analysis on each arc in Fig. 5.

We also estimated the radiative age trend by assuming the reference equipartition magnetic field from the formula provided by Govoni & Feretti (2004, Eq. (22)), which derives from the classical equipartition formula (Pacholczyk 1970) that is obtained for a power law energy distribution of electrons. However, we detect a synchrotron spectrum whose properties are affected by radiative ageing. In order to correct for this effect, we estimated the spectrum of the arcs at lower frequencies, where ageing is not important and the assumption of power-law energy distribution is satisfied. In particular, we calculated the emission at a frequency of 100 MHz by re-scaling the spectrum measured at 1.4 GHz according to the synchrotron spectrum with a break frequency derived from the spectral slope between 1.4 GHz and 3.0 GHz, obtaining an estimated flux density at

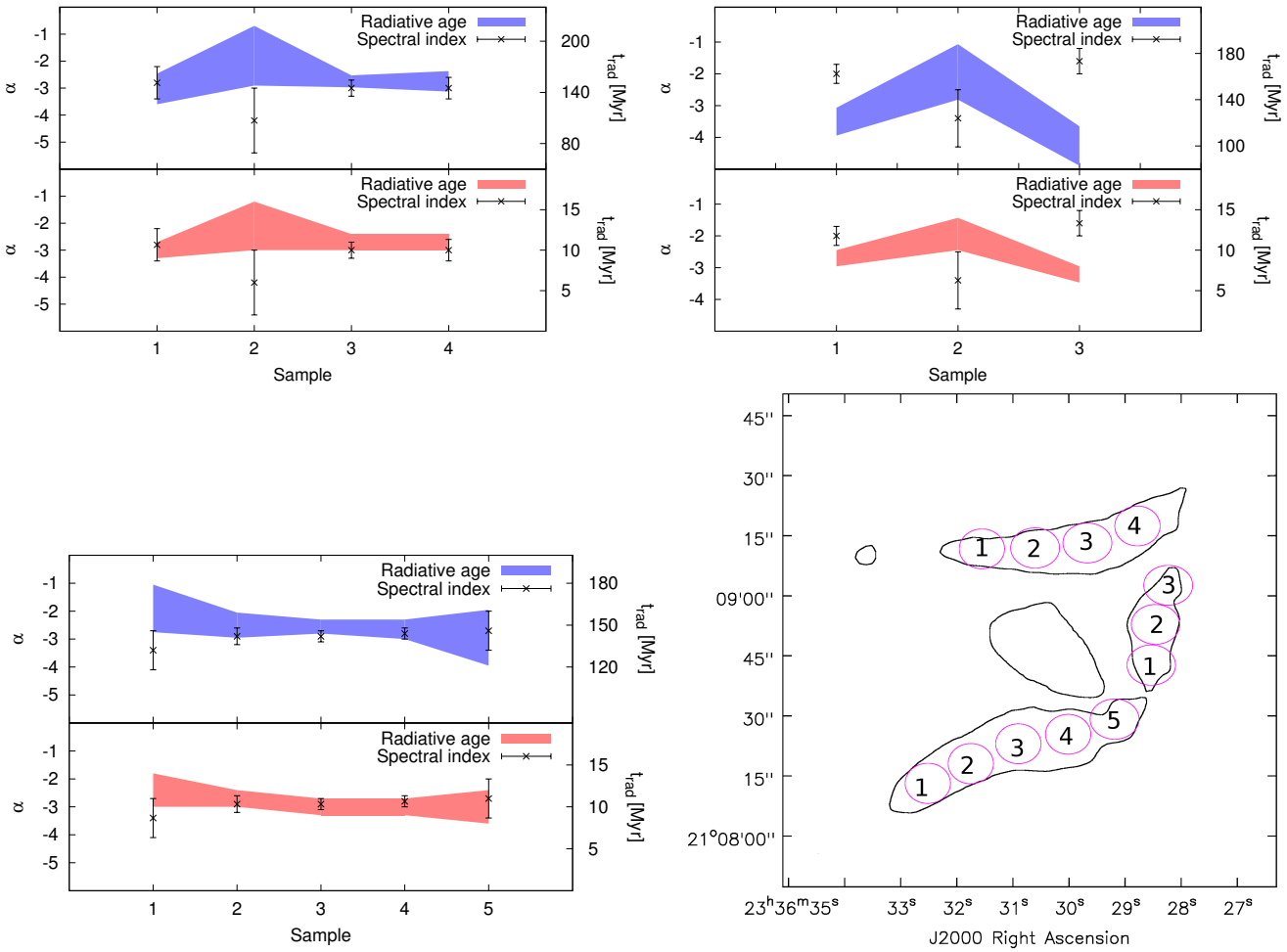

Fig. 5. Spectral index and radiative age trend along the radio arcs obtained with the sampling method shown in the *bottom-right panel*. On the *x*-axis is shown the sampling numeration (indicated in the *bottom right panel*), on the left *y*-axis the spectral index scale and on the right *y*-axis the radiative age scale. In each panel the top blue plot displays the radiative age estimated by assuming $B = B_{ml} = 2.1$ μG, and the bottom red plot displays the radiative age estimated by assuming the equipartition magnetic field $B = B_{\rm eq} = 12$ μG. *Top-left*: northern arc trends; *top-right*: western arc trends; *bottom-left*: southern arc trends; *bottom-right*: sampling method. The black contours are the 1.4 GHz reference levels reported in Fig. 2, *middle panel*.

100 MHz of ∼260 mJy. By assuming that the spectral index of the arcs at ≤100 MHz is ∼−0.7, that the arcs have a cylindrical volume, and that the energy in electrons and protons is equally distributed ($k = 1$), we estimated a equipartition field strength of $B_{eq} = 12$ μG. Depending on the magnetic field, the mean radiative age of the arcs decreases from ∼140 Myr to ∼10 Myr, whereas the mean error on it decreases from ∼10 Myr to ∼1 Myr. Due to the uncertainties in the assumptions made to derive the equipartition magnetic field, in the following discussion we consider the estimates of radiative age upper limits provided by B_{ml}.

The plots in Fig. 5 show that the radio arcs do not exhibit significant trends in spectral index or radiative age. By considering the uncertainties of our measures, we derived an estimate of the maximum difference between the radiative timescale $\Delta t_{\rm rad}$ of 22 Myr, 26 Myr and 22 Myr for the northern, southern, and western arcs, respectively. This corresponds to an estimate of the upper limit on the time required by the jets to cover the arc length.

In order to test the jet-precession model, we compared our result with a theoretical estimate of the precession period. Wong et al. (2008) argued that the jet precession may be triggered by the mutual gravitational interactions of the optical cores of IC 5338. The precession period, $\tau_{\rm prec}$, of the jets of a binary system in the center of a galaxy cluster can be estimated with the relation proposed by Pizzolato & Soker (2005). We re-scaled the relation that they provide according to the parameters that we observe:

$$\tau_{\rm prec} = 1.6\times10^{4}\left(\frac{M}{10^{8}\,M_{\odot}}\right)^{-1/2}\left(\frac{a}{1\ {\rm kpc}}\right)^{3}\left(\frac{a_{\rm D}}{1\ {\rm pc}}\right)^{-3/2}\frac{(1+q)^{1/2}}{q\,\cos\theta}\,{\rm Gyr}, \quad (2)$$

where M and q are the sum and the ratio of the masses of the black holes, respectively, a is their distance, $a_{\rm D}$ is the radius of the accretion disk and θ is the angular difference between the accretion disk and the plane of the orbit of the black holes. In the case of A2626, the masses of the objects and the accretion disk radius are unknown, so we assumed a mass of 10^8 $M_{\odot}$ (so $M = 2\times10^8$ $M_{\odot}$, $q = 1$), that is, the typical mass of the supermassive black holes (SMBH) located at the center of cD galaxies, and the typical accretion disk radius $a_{\rm D} = 1$ pc. The observed projected distance between the cores, which is a lower limit to their real distance, is $a \sim 4$ kpc. Moreover, θ is also unknown, therefore we assume for simplicity that the accretion disk is on the same plane as the orbit ($\theta = 0$). From these assumptions, we estimated a lower limit for the precession time $\tau_{\rm prec} \gtrsim 10^5$ Gyr, that is not

in agreement with the $\Delta t_{\rm rad}$ that we measure. This estimate is also much greater than the age of the Universe, thus challenging the hypothesis that the two nuclei are currently producing the jet-precession. More specifically, from the formula proposed by Pizzolato & Soker (2005), the distance between the two cores that admit a precession period $\tau_{\rm prec} \simeq \Delta t_{\rm rad}$ is:

$$a \leq 10 \left(\frac{\tau}{20\,\mathrm{Myr}}\right)^{1/3} \left(\frac{M}{10^8\,M_\odot}\right)^{1/6} \left(\frac{a_{\rm d}}{1\,\mathrm{pc}}\right)^{1/2} \left(\frac{q\cos\theta}{(1+q)^{1/2}}\right)^{1/3} \mathrm{pc}. \quad (3)$$

Consequently, at the epoch of particle acceleration (corresponding to $t_{\rm rad} \approx 150$ Myr ago), the two cores had to have a separation of only a few pc. Alternatively, the precession should have been generated by the interactions with a secondary SMBH that is yet undetected (likely not active), rather than with the northern optical core of IC 5338. Therefore, we argue that the dynamical process behind the origin of the radio arcs may be more complex than the scenario initially proposed by Wong et al. (2008). At the same time, however, the lack of a clear optical core candidate makes the precession model less appealing, and other scenarios for the origin of the radio arcs should be investigated in the future.

We finally note that by combining the results of our spectral analysis with the spectral maps provided by Kale & Gitti (2017), we may argue that the radio spectrum of the arcs has a steep spectral index <-2.5 from 610 MHz to 3 GHz, not in agreement with the expected evolution of the radio spectrum of the hot-spots. The AGN-driven nature of the radio arcs through jet precession may be further challenged by the fact that we observe four arcs, which would require the presence of two pairs of radio jets, powered by two radio cores inside IC 5338. However, only one radio AGN (with jets) is currently observed, and a potential second one remains undetected (although it is still possible that it was active in the past and has recently shut down).

5. Summary and conclusion

We present the results of new JVLA observations of A2626 at 3 GHz and 5.5 GHz, which were requested in order to test the jet-precession model for the origin of the radio arcs. We have achieved the first detection at high frequency of an extended component of radio emission at 5.5 GHz and have observed for the first time the radio arcs at 3 GHz. Moreover, we have observed the extended emission of IC 5337 at 3 GHz and 5.5 GHz.

By combining the archival 1.4 GHz observation (G13) with the new one at 3 GHz, we have produced new spectral index maps that have allowed us to disentangle the extended emission of the cluster in two main components – the inner, flat-spectrum emission ($\alpha \simeq -0.7$), and the ultra-steep spectrum ($\alpha \leq -2.5$) arcs. In order to find constraints for the jet-precession model, we converted the spectral index map into radiative age maps and studied the trends of spectral index and radiative time along the arcs. We find that the radio arcs do not exhibit significant spectral index or radiative age evolution. By considering the uncertainties on our measures, we estimate an upper limit of the precession period $\Delta t_{\rm rad} \leq 26$ Myr. We also estimate a mean radiative age of $t_{\rm rad} \leq 150$ Myr, that may be considered as a measure of the time elapsed since the hot-spot ceased to accelerate the particles.

We then compared our results with a theoretical precession period estimated for the current kinematics of the IC 5338 system and find a disagreement. Therefore, we argue that the dynamics of the cores that produced the jet-precession and created the radio arcs may be more complex than the scenario proposed by Wong et al. (2008). On the other hand, our results put strong constraints for every future model relating the origin of the radio arcs to the activity of the inner AGN, or indicating a different origin of the radio arcs.

Acknowledgements. We thank the referee for the prompt response and constructive comments. A.I. thanks R. Paladino for helpful advice during the data reduction with CASA. We thank A. Bonafede, M. Bondi and D. Dallacasa for useful discussions. M.G., G.B., G.G., L.F. acknowledge partial support from PRIN-INAF 2014.

References

Bravi, L., Gitti, M., & Brunetti, G. 2016, MNRAS, 455, L41
Brunetti, G., & Jones, T. W. 2014, Int. J. Mod. Phys. D, 23, 30007
Condon, J. 2015, ArXiv e-prints [arXiv:1502.05616]
Doria, A., Gitti, M., Ettori, S., et al. 2012, ApJ, 753, 47
Feretti, L., Giovannini, G., Govoni, F., & Murgia, M. 2012, A&ARv, 20, 54
Gitti, M. 2013, MNRAS, 436, L84
Gitti, M., Brunetti, G., & Setti, G. 2002, A&A, 386, 456
Gitti, M., Brunetti, G., Feretti, L., & Setti, G. 2004, A&A, 417, 1
Gitti, M., Brighenti, F., & McNamara, B. R. 2012, Adv. Astron., 2012, 950641
Gitti, M., Giroletti, M., Giovannini, G., Feretti, L., & Liuzzo, E. 2013, A&A, 557, L14
Govoni, F., & Feretti, L. 2004, Int. J. Mod. Phys. D, 13, 1549
Kale, R., & Gitti, M. 2017, MNRAS, 466, L19
Meisenheimer, K., Yates, M. G., & Roeser, H.-J. 1997, A&A, 325, 57
Mohr, J. J., Geller, M. J., & Wegner, G. 1996, AJ, 112, 1816
Murgia, M., Fanti, C., Fanti, R., et al. 1999, A&A, 345, 769
Pacholczyk, A. G. 1970, Radio astrophysics. Nonthermal processes in galactic and extragalactic sources, ed. A. G. Pacholczyk (San Francisco: Freeman & Co Ltd)
Pizzolato, F., & Soker, N. 2005, Adv. Space Res., 36, 762
Poggianti, B. M., Fasano, G., Omizzolo, A., et al. 2016, AJ, 151, 78
Rau, U., & Cornwell, T. J. 2011, A&A, 532, A71
Struble, M. F., & Rood, H. J. 1999, ApJS, 125, 35
Wong, K.-W., Sarazin, C. L., Blanton, E. L., & Reiprich, T. H. 2008, ApJ, 682, 155